reach the thermodynamic equilibrium under our reaction conditions, the final concentrations of all the four compounds should be the same in both experiments. The experimental results matched the prediction very well, and nearly identical final concentrations of all the four reaction components were obtained in both experiments. Thus, we can conclude that the reaction of these substrates is reversible and that thermodynamic equilibrium can be reached under our normal reaction conditions. Collectively, these preliminary mechanistic experiments strongly support the proposed transfer mechanism shown in Fig. 1B.

In a broader context, the functional group metathesis strategy delineated in this work will likely stimulate the development of reversible hydrofunctionalization reactions of alkenes that elude the use of hazardous gases in the laboratory.

REFERENCES AND NOTES

1. P. Pollak, G. Romeder, F. Hagedorn, H. Gelbke, "Nitriles," in *Ullman's Encyclopedia of Industrial Chemistry* (Wiley-VCH, Weinheim, Germany, ed. 5, 1985), vol. A17, p. 363.
2. M. B. Smith, J. March, *March's Advanced Organic Chemistry: Reactions, Mechanisms, and Structure* (Wiley-Interscience, Hoboken, NJ, ed. 6, 2007).
3. S. Patai, J. Zabicky, Eds., "The Alkenes: Volumes 1 and 2," in *PATAI's Chemistry of Functional Groups* (Wiley, 1964/1970).
4. R. H. Grubbs, *Handbook of Metathesis* (Wiley-VCH, Weinheim, Germany, 2003).
5. W. C. Drinkard Jr., US 3496218A, **1970**.
6. P. W. N. M. van Leeuwen, *Homogeneous Catalysis: Understanding the Art* (Springer, Netherlands, 2004), chap. 5.
7. J. F. Hartwig, *Organotransition Metal Catalysis* (Palgrave Macmillan, 2009), pp. 668–676.
8. L. Bini, C. Müller, D. Vogt, *ChemCatChem* **2**, 590–608 (2010).
9. A. L. Casalnuovo, T. V. Rajanbabu, "Transition-metal-catalyzed alkene and alkyne hydrocyanations," in *Transition Metals for Organic Synthesis: Building Blocks and Fine Chemicals*, M. Beller, C. Bolm, Eds. (Wiley-VCH, 2008), chapter 2.5.
10. M. Beller, J. Seayad, A. Tillack, H. Jiao, *Angew. Chem. Int. Ed.* **43**, 3368–3398 (2004).
11. T. V. Rajanbabu, *Org. React.* **75**, 1–74 (2011).
12. C. A. Tolman, R. J. Mckinney, W. C. Seidel, J. D. Druliner, W. R. Stevens, *Adv. Catal.* **33**, 1–46 (1985).
13. C. A. Tolman, W. C. Seidel, J. D. Druliner, P. J. Domaille, *Organometallics* **3**, 33–38 (1984).
14. J. E. Bäckvall, O. S. Andell, *Organometallics* **5**, 2350–2355 (1986).
15. N. M. Brunkan, D. M. Brestensky, W. D. Jones, *J. Am. Chem. Soc.* **126**, 3627–3641 (2004).
16. B. Gaspar, E. M. Carreira, *Angew. Chem. Int. Ed.* **46**, 4519–4522 (2007).
17. S. L. Buchwald, S. J. LaMaire, *Tetrahedron Lett.* **28**, 295–298 (1987).
18. G. Romeder, Hydrogen Cyanide. *e-EROS Encyclopedia of Reagents for Organic Synthesis* (2001).
19. HCN LD_{50} (intravenous): 1.1 mg/Kg. *Medical Management of Chemical Casualties Handbook*. United States Army Medical Research Institute of Chemical Defense (USAMRICD).
20. M. de Greef, B. Breit, *Angew. Chem. Int. Ed.* **48**, 551–554 (2009).
21. M. J. Baker, P. G. Pringle, *J. Chem. Soc. Chem. Commun.* **18**, 1292–1293 (1991).
22. A. Falk, A.-L. Göderz, H.-G. Schmalz, *Angew. Chem. Int. Ed.* **52**, 1576–1580 (2013).
23. S. A. Haroutounian, Acetone cyanohydrin. *e-EROS Encyclopedia of Reagents for Organic Synthesis* (2001).
24. W. C. Groutas, Cyanotrimethylsilane. *e-EROS Encyclopedia of Reagents for Organic Synthesis* (2001).
25. A. L. Casalnuovo, T. V. Rajanbabu, T. A. Ayers, T. H. Warren, *J. Am. Chem. Soc.* **116**, 9869–9882 (1994).
26. W. Goertz *et al.*, *J. Chem. Soc., Dalton Trans.* **18**, 2981–2988 (1998).
27. D. R. Lide, Ed., *CRC Handbook of Chemistry and Physics, Internet Version 2005* (CRC Press, Boca Raton, FL, 2005).
28. Heat of formation (*27*) of ethene (52.4 KJ/mol), HCN (135.1 KJ/mol), and propanenitrile (51.7 KJ/mol) indicate that hydrocyanation is exothermic whereas retro-hydrocyanation is endothermic.
29. C. R. Landis, *Science* **347**, 29–30 (2015).
30. Y. J. Park, J.-W. Park, C.-H. Jun, *Acc. Chem. Res.* **41**, 222–234 (2008).
31. S. K. Murphy, J.-W. Park, F. A. Cruz, V. M. Dong, *Science* **347**, 56–60 (2015).
32. S. Kusumoto, T. Tatsuki, K. Nozaki, *Angew. Chem. Int. Ed.* **54**, 8458–8461 (2015).
33. A. S. Goldman *et al.*, *Science* **312**, 257–261 (2006).
34. G. E. Dobereiner, R. H. Crabtree, *Chem. Rev.* **110**, 681–703 (2010).
35. J. R. Zbieg, E. Yamaguchi, E. L. McInturff, M. J. Krische, *Science* **336**, 324–327 (2012).
36. Y. Nakao, A. Yada, S. Ebata, T. Hiyama, *J. Am. Chem. Soc.* **129**, 2428–2429 (2007).
37. A. Yada, T. Yukawa, H. Idei, Y. Nakao, T. Hiyama, *Bull. Chem. Soc. Jpn.* **83**, 619–634 (2010).
38. P. R. Khoury, J. D. Goddard, W. Tam, *Tetrahedron* **60**, 8103–8112 (2004).
39. J. C. Lo, Y. Yabe, P. S. Baran, *J. Am. Chem. Soc.* **136**, 1304–1307 (2014).
40. Y. Liu, S. C. Virgil, R. H. Grubbs, B. M. Stoltz, *Angew. Chem. Int. Ed.* **54**, 11800–11803 (2015).

ACKNOWLEDGMENTS

We thank Z. K. Wickens (Harvard University) and R. H. Grubbs (California Institute of Technology) for critical proofreading of this manuscript. Generous funding from the Max-Planck-Society and the Max-Planck-Institut für Kohlenforschung is acknowledged. We thank B. List for sharing analytical equipment, and our nuclear magnetic resonance, gas chromatography, and mass spectrometry departments for technical assistance. P.Y. thanks the China Scholarship Council for a scholarship. A provisional patent application has been filed on this reaction.

SUPPLEMENTARY MATERIALS

www.sciencemag.org/content/351/6275/832/suppl/DC1
Materials and Methods
Fig. S1
Tables S1 and S2
References (*41*–*66*)

14 December 2015; accepted 19 January 2016
10.1126/science.aae0427

APPLIED PHYSICS

Nuclear magnetic resonance detection and spectroscopy of single proteins using quantum logic

I. Lovchinsky,[1] A. O. Sushkov,[1,2]* E. Urbach,[1] N. P. de Leon,[1,2]† S. Choi,[1] K. De Greve,[1] R. Evans,[1] R. Gertner,[2] E. Bersin,[1] C. Müller,[3] L. McGuinness,[3] F. Jelezko,[3] R. L. Walsworth,[1,4,5] H. Park,[1,2,5,6]‡ M. D. Lukin[1]‡

Nuclear magnetic resonance spectroscopy is a powerful tool for the structural analysis of organic compounds and biomolecules but typically requires macroscopic sample quantities. We use a sensor, which consists of two quantum bits corresponding to an electronic spin and an ancillary nuclear spin, to demonstrate room temperature magnetic resonance detection and spectroscopy of multiple nuclear species within individual ubiquitin proteins attached to the diamond surface. Using quantum logic to improve readout fidelity and a surface-treatment technique to extend the spin coherence time of shallow nitrogen-vacancy centers, we demonstrate magnetic field sensitivity sufficient to detect individual proton spins within 1 second of integration. This gain in sensitivity enables high-confidence detection of individual proteins and allows us to observe spectral features that reveal information about their chemical composition.

Conventional nuclear magnetic resonance (NMR) spectroscopy relies on detecting the weak magnetization of a thermally polarized ensemble of nuclear spins and therefore typically requires high magnetic fields and macroscopic sample quantities (*1*). Recently, it has been shown that single nitrogen-vacancy (NV) color centers in diamond can serve as atomic-sized magnetometers that are capable of label-free detection of the statistical nuclear polarization of nanoscale ensembles (*2*, *3*), and even single nuclear spins (*4*), under ambient conditions (*5*, *6*). Our method is based on the coherent control of an individual NV center, which is a localized defect in the diamond lattice consisting of a substitutional nitrogen atom and an adjacent vacancy in the carbon lattice. The spin state of the negatively charged NV center has an exceptionally long coherence time, even at room temperature, and its electronic level structure allows efficient, all-optical spin polarization

[1]Department of Physics, Harvard University, Cambridge, MA 02138, USA. [2]Department of Chemistry and Chemical Biology, Harvard University, Cambridge, MA 02138, USA. [3]Institute for Quantum Optics and Center for Integrated Quantum Science and Technology (IQST), Ulm University, D-89081, Ulm, Germany. [4]Harvard-Smithsonian Center for Astrophysics, Cambridge, MA 02138, USA. [5]Center for Brain Science, Harvard University, Cambridge, MA 02138, USA. [6]Broad Institute of MIT and Harvard, 7 Cambridge Center, Cambridge, MA 02142, USA. *Present address: Department of Physics, Boston University, 590 Commonwealth Avenue, Boston, MA 02215, USA. †Present address: Department of Electrical Engineering, Princeton University, Olden Street, Princeton, NJ 08544, USA. ‡**Corresponding author. E-mail: lukin@physics.harvard.edu (M.D.L.); hongkun_park@harvard.edu (H.P.)**

Downloaded from on February 22, 2016

and readout. In our approach (Fig. 1), we measure individual Fourier components of the time-varying magnetic field created by a statistically polarized subset of proximal nuclear spins contained within a protein. The transverse magnetization of the spin ensemble undergoes precession at the nuclear Larmor frequency with a phase and amplitude that vary stochastically with every repetition of the sequence. Averaging over many iterations yields a zero mean magnetization but a nonzero variance, which results in a measurable magnetic resonance signal. To use the NV center as a sensor, its spin state is manipulated with a series of periodic microwave pulses separated by free-evolution intervals of length τ (Fig. 1B). This periodic modulation of the NV center spin creates a narrow band-pass frequency filter, allowing phase accumulation when the modulation frequency, defined as $1/\tau$, is close to twice the nuclear Larmor frequency (*5*, *7*, *8*). Varying the spacing between the π pulses yields a frequency spectrum that encodes information about the nuclear spins within the protein. Assuming that the spins are situated on the diamond surface at distance d directly above the NV center, the optimal sensitivity of this technique (defined by the minimum number N of nuclear spins detectable after 1 s of integration) is achieved when the pulse-sequence duration is approximately equal to the coherence time T_2 of the NV electronic spin (*5*) [see (*8*) for derivation]

$$N \approx \frac{16\pi^4 d^6}{(\mu_0 \hbar \gamma_e \gamma_n)^2 \mathcal{F}} \frac{\sqrt{T_2 + T_R}}{T_2^2}$$

Here, $\gamma_e = 1.76 \times 10^{11}$ s^{-1} T^{-1} and γ_n are the electron and nuclear gyromagnetic ratios (for proton spins $\gamma_n = 2.68 \times 10^8$ s^{-1} T^{-1}), d is the NV center depth, μ_0 is the vacuum permeability, $\hbar$ is Planck's constant h divided by 2π, and T_R is the readout time. The readout fidelity $\mathcal{F} = [1 + 2(\alpha_0 + \alpha_1)/(\alpha_0 - \alpha_1)^2]^{-\frac{1}{2}}$ is determined by the mean number of photons α_0, α_1 detected per shot from the $m_s = 0$ and 1 spin sublevels of the NV center, respectively. The readout fidelity encapsulates the effect of photon shot noise and approaches unity for an ideal, projection noise-limited measurement.

One limitation to the sensitivity is due to the imperfect readout of the NV center. For typical fluorescence collection efficiencies, $\mathcal{F} \approx 0.03$ (*8*). Thus, ~10^3 repetitions of the experiment are required to distinguish the fluorescence of the $m_s = 0$ and ± 1 sublevels. To circumvent this imperfection, we use a two-qubit quantum system consisting of an NV center electronic spin and its associated ^{15}N nuclear spin, such that after the sensing sequence, the resulting NV spin can be repeatedly probed without resetting its state via optical pumping (*9*, *10*). We use quantum logic (Fig. 1B) to manipulate the two coupled qubits and to improve readout fidelity [see (*8*) for details]. The experimentally measured gain in the readout fidelity as a function of readout cycles (Fig. 1C, red points) demonstrates an almost 10-fold improvement for several hundred repetitions, as compared with conventional readout (dashed blue line). Although repetitive readout of the electronic spin state leads to an increase in the readout time T_R (*8*), the sensitivity is only weakly dependent on this variable. Therefore, in the regime where T_R is on the order of T_2, we achieve a significant gain in sensitivity.

Another key limitation to the sensitivity is attributable to the decoherence of near-surface NV centers (i.e., those with small d) (*11*). To quantify the effect of the surface on the NV spin coherence, we measure the decoherence rates ($1/T_2$) and depths (*8*) for a large number of NV centers created by implantation of 2-keV ^{15}N ions. As shown in table S1, the depths and decoherence rates of shallow NV centers are inversely correlated. To improve the coherence properties, we use wet oxidative chemistry combined with annealing at 465°C (*12*, *13*) in a dry oxygen environment (*8*). This procedure etches away the diamond surface while improving the coherence times by more than an order of magnitude. When combined with the 10-fold improvement in readout fidelity resulting from quantum logic–based readout, this increase in T_2 yields shallow (3 to 6 nm) NV centers with an overall sensitivity gain greater than a factor of 500 (Fig. 2A), exceeding sensitivities reported in previous experiments (fig. S2). The resulting sensitivity is sufficient to detect a single proton spin or ~10 statistically polarized ^{13}C or ^{2}H spins after 1 s of integration (Fig. 2A) (*8*).

We use our enhanced sensitivity to probe ubiquitin, a small regulatory protein consisting of 76 residues that is found in almost all eukaryotic cells (*14*). The size of this protein (*15*) is on the

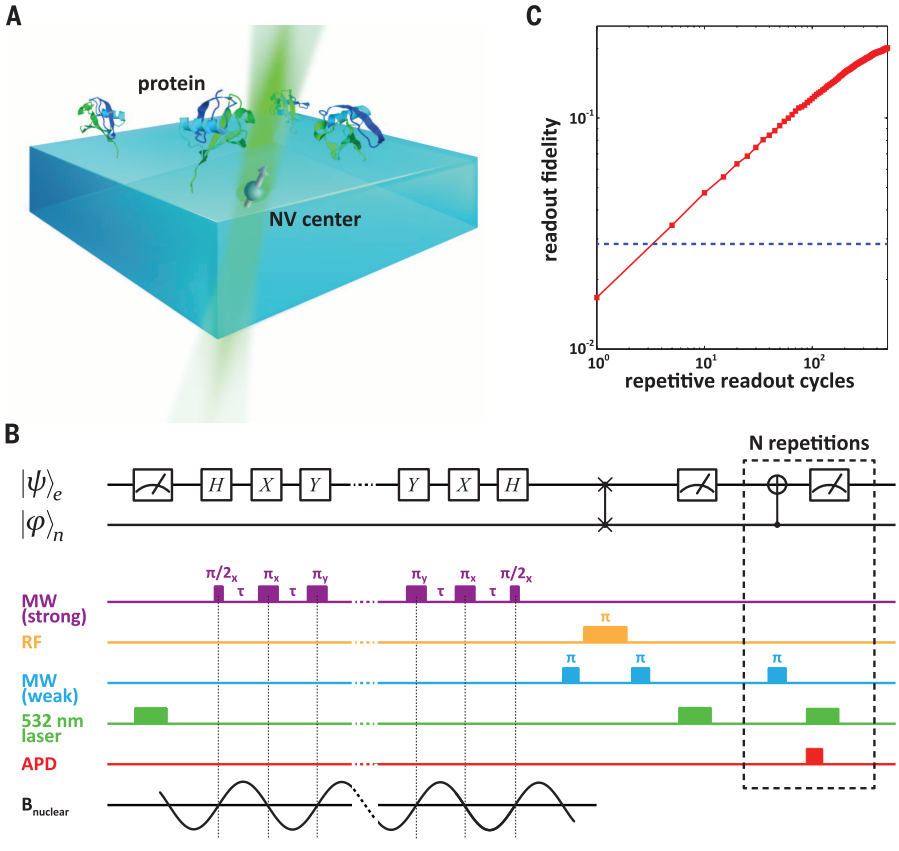


Fig. 1. Experimental setup and magnetometry with repetitive readout. (**A**) Schematic of the experimental setup. Ubiquitin proteins attached to the diamond surface are probed using a proximal quantum sensor consisting of a NV center electronic spin and its associated ^{15}N nuclear spin. The image of ubiquitin was taken from the Protein Data Bank (PDB ID: 1UBQ) (*15*). (**B**) Quantum circuit diagram and experimental magnetometry pulse sequence. Here the NMR signal is measured using a modified XY8-k dynamical decoupling sequence (*8*) and detected using repetitive readout of the electronic spin state. $|\psi\rangle_e$ and $|\varphi\rangle_n$ correspond to the electric and nuclear spin states, respectively. MW and RF correspond to microwave and radio frequency drive fields, respectively. APD denotes the photodetector used for optical measurement. $B_{nuclear}$ corresponds to the magnetic field created by the target nuclear spins. (**C**) Measured gain in the readout fidelity $\mathcal{F}$ as a function of repetitive readout cycles (red curve). The dashed blue line indicates the measured fidelity using conventional readout. The readout fidelity is measured by detecting the average number of photons scattered from the NV center after preparing it in the $m_s = 0$ or 1 sublevel and applying eq. S9 (*8*).

order of the NV detection area/volume (*8*), determined by the NV center depth for $d \sim 3$ to 5 nm. Thus, any observed NMR signals can be attributed to individual or small aggregates of proteins. We immobilize the proteins on the diamond surface by means of carbodiimide cross-linker chemistry (*16*, *17*) [see also Fig. 2B and (*8*)]. We then use atomic force microscopy (AFM) to characterize the topography of the diamond surface after protein attachment (*8*). The AFM images (Fig. 2C) exhibit circular features with heights and radii (Fig. 2D) that are consistent with the known size of the protein. We observe almost no features with height larger than 5 nm, suggesting that our attachment protocol does not lead to aggregation. The resolution in the lateral dimensions is consistent with the limit imposed by the radius of the AFM probe (9 ± 2 nm). We confirm that individual spots in Fig. 2C mostly correspond to individual proteins by conjugating the proteins to Cy3 fluorophores and comparing the resulting mean fluorescence rate with that of optically resolved Cy3+ubiquitin complexes and individual Cy3 dye molecules (*8*). We find that the mean protein spacing, as extracted from optical measurements (20.9 ± 1.4 nm), is in excellent agreement with that based on AFM measurements (21.6 ± 0.4 nm). Importantly, these measurements show that the mean spacing of the proteins is much greater than the typical NV center depth ($d \approx 4$ nm) and the protein size. Due to the strong $\sim 1/r^6$ dependence of the NMR contrast on the NV-protein separation r (*8*), the NMR signal is negligible for proteins located far outside the NV detection area. Therefore, with our protein density, we expect ~10% of NV centers to contain a single protein within their detection areas. The statistical probability of detecting two or more proteins using a single NV center is ~1% (*8*).

To spectrally differentiate the magnetic fields produced by protein nuclear spins from background sources—such as ^{1}H spins on the diamond surface (*18*) and ^{13}C spins in the diamond lattice—we use diamond samples enriched in ^{12}C (99.999% abundance) and proteins enriched in the rare isotopes ^{2}H and ^{13}C (both at >98% abundance). We first carried out NMR measurements on 20 shallow NV centers, with isotopically enriched ubiquitin proteins attached to the diamond surface. Three of the NV probes exhibited NMR signals at both the ^{2}H and ^{13}C Larmor frequencies (*8*). No instances occurred in which only one of these nuclear species was detected. Representative spectra (Fig. 3, A and B) were obtained by varying the spacing of the periodic π pulses. Here, the data were normalized to subtract the effect of NV decoherence (*8*). The ^{2}H and ^{13}C spectra were acquired using XY8-507 and XY8-1011 pulse sequences (*8*), respectively, and measured via 500 repetitive readout cycles. The identities of the nuclear species were verified by observing the linear scalings of the nuclear Larmor frequencies with the applied magnetic field (Fig. 3C, blue and red points).

The spectral resolution Δν of the present method is Fourier-limited by the total duration of the coherent evolution of the quantum spin sensor (Fig. 3D). Note that the 10-fold increase in the coherence time T_2 demonstrated in Fig. 2A directly yields a corresponding 10-fold improvement in spectral resolution (*8*), allowing us to resolve features in the protein spectra and revealing information about its chemical composition.

Figure 3E shows the ^{2}H and ^{13}C NMR spectra (top two panels), corresponding to ubiquitin proteins enriched with ^{2}H and ^{13}C, performed on another NV center. Consistent with the results of Fig. 3, A and B, for the first NV center, we find that the deuterium spectrum exhibits an extremely broad line shape, whereas the ^{13}C spectral width is considerably narrower and is consistent with the Fourier limit. The bottom panel in Fig. 3E shows the ^{13}C NMR spectrum after attaching ubiquitin proteins enriched only in ^{13}C.

We observe a ^{13}C line shape that is significantly broader (~20 kHz) than that of the deuterated proteins. The spectral resolution, determined by the external magnetic field and the number of applied π pulses, is indicated by the shaded green regions in Fig. 3. Figure 3F shows the average deconvolved spectral widths of ^{2}H and ^{13}C, as observed in independent measurements of three NV centers with deuterated proteins and three NV centers with nondeuterated proteins.

Previous studies (*19*) have shown that solid-state ^{2}H NMR spectra typically exhibit line broadening due to the inhomogeneous distribution of quadrupole shifts within the protein

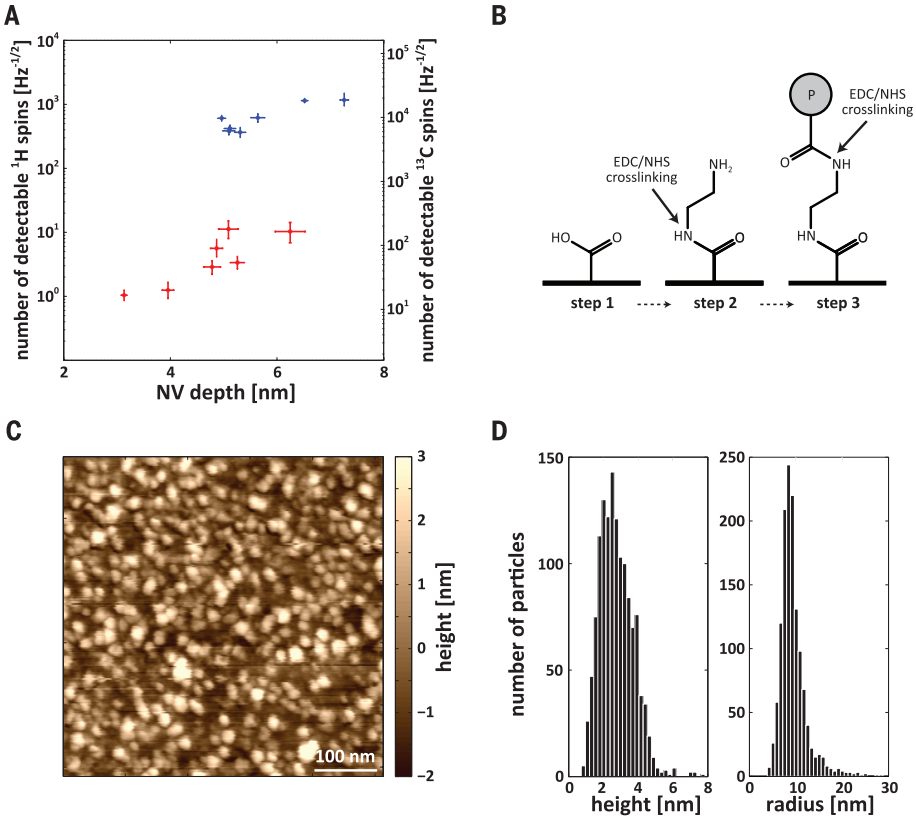


Fig. 2. Surface preparation of diamond samples and single-protein attachment. (**A**) Measured depths and sensitivities (^{1}H and ^{13}C spins) for a representative sample of NV centers before (blue) and after (red) oxygen surface treatment and quantum logic–based readout. See table S1 for numerical values of measured depths and decoherence rates. (**B**) Attachment protocol using carbodiimide cross-linker chemistry (*8*). EDC, 1-ethyl-3-(3-dimethylaminopropyl) carbodiimide; NHS, *N*-hydroxysuccinimide. (**C**) AFM height image of diamond surface after protein attachment. The color bar indicates height values. (**D**) Histograms of heights and radii of circular features in a 1 μm–by–1 μm AFM image (*8*).

(*20*) (see also Fig. 4A). The broadening of our ^{2}H spectra is consistent with this effect. Our ^{2}H NMR signals are probably dominated by the deuterons in methyl groups, which rotate rapidly at room temperature about the methyl group symmetry axis. The remaining (nonaveraged) quadrupolar shifts are on the order of 30 kHz (*19*) (the deuterons in other chemical groups, such as methylene or aromatic groups, give rise to much broader spectral features and, hence, smaller signals). The ^{13}C linewidths are consistent with the expected broadening created by dipolar interactions with proximal ^{2}H (in deuterated proteins) and ^{1}H (in nondeuterated proteins) spins (*19*), with ^{1}H giving rise to broader linewidths due to its larger gyromagnetic ratio.

Our method can be extended in a number of ways. The sensitivity can be further improved by using spin-to-charge readout (*21*) or more advanced pulse sequences that could extend the coherence time to the limit imposed by the population relaxation time T_1 (see, for example, fig. S2B, which shows coherent spin locking for up to 1 ms). Nuclear hyperpolarization (*8*), such as Hartmann-Hahn double resonance (*22*), can also be used to improve sensitivity via direct detection of nuclear magnetic moments rather than their variances. Alternatively, reporter spin–based sensing can be used to reach single-spin sensitivity by resolving individual nuclear spins in a field gradient created by an electronic reporter spin (*4*). Similarly, if background protons can be removed from the diamond surface [protons in liquid water diffuse quickly and do not contribute to the NMR signal (*23*)] by deuteration (*3*), ^{1}H spins, with their large gyromagnetic ratio, can be used for indirect detection of nuclei with low magnetic moments (*24*). In addition, the coupling to a long-lived quantum memory associated with an ancillary nuclear spin qubit and the use of new pulse sequences (*4*, *25*) should allow further improvement in spectral resolution to the limit determined by the lifetime of the nuclear spin ancilla, which could be >10 mHz (*6*). Independently of the NV and nuclear spin manipulation, the detection sensitivity and utility of the method can be greatly enhanced by deterministically positioning the molecules in close proximity to

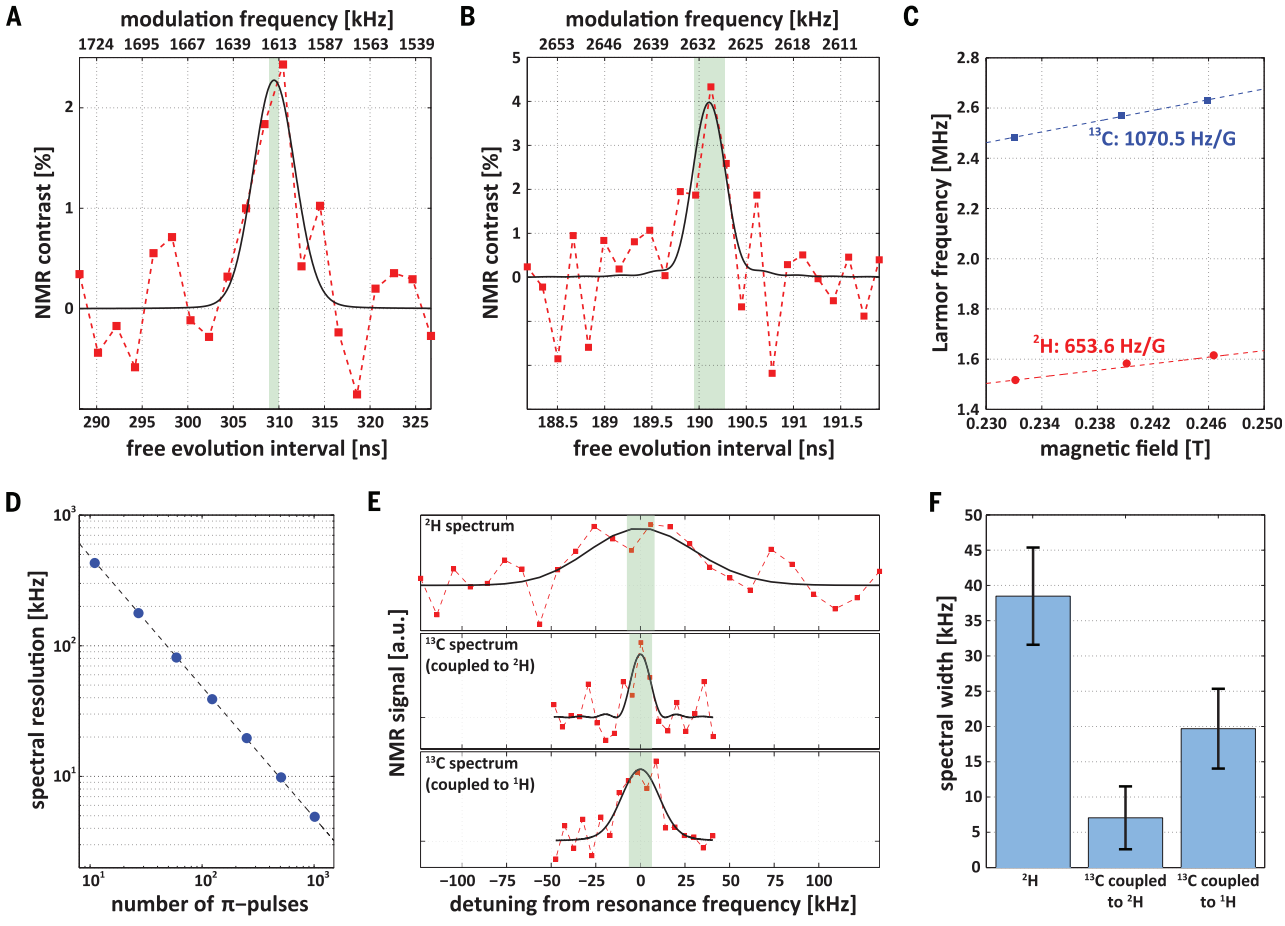


Fig. 3. NMR detection and spectroscopy of individual ubiquitin proteins. (**A**) ^{2}H NMR spectrum at magnetic field B = 2473 G, using the XY8-507 sequence with 500 repetitive readout cycles (red points) and Gaussian fit (black solid line). The spectrum consists of the NV optical signal, normalized by the Rabi contrast and corrected for the reduced contrast caused by decoherence (*8*). (**B**) Analogous ^{13}C NMR spectrum at B = 2457 G, using the XY8-1011 sequence with 500 repetitive readout cycles (red points) and Gaussian fit (black solid line). (**C**) Scalings of resonance frequencies with applied magnetic field. Red and blue points indicate the ^{2}H and ^{13}C resonances, respectively (*8*). The expected scalings based on the known gyromagnetic ratios are indicated with dashed lines. Error bars are approximately on the scale of the marker sizes. (**D**) Measured spectral resolution (blue points) as a function of the number of π pulses. The dashed black line indicates the theoretical limit imposed by the detector filter function (*8*). A 2.63-MHz radio frequency waveform, corresponding to τ = 190 ns and applied using an external coil, was used as the calibration signal. The resulting NMR signal was measured using an XY8 sequence. (**E**) ^{2}H and ^{13}C NMR linewidths (red points) measured on deuterated (top and middle panels) and nondeuterated (bottom panel) ubiquitin proteins. B = 2422 G (top), 2402 G (middle), and 2455 G (bottom). a.u., arbitrary units. In (A), (B), and (E), fitted curves are Gaussian functions, convolved with the detector filter function. Green shaded regions correspond to the spectral resolution (*8*). (**F**) Average spectral widths from several independent measurements of ^{2}H and ^{13}C NMR spectra (*8*). Here, the observed spectra have been deconvolved from the detector filter function to yield the true linewidths [as extracted from fits presented in (*8*)]. Error bars correspond to SEM of the spectral widths, for each of the three categories of spectra. For all ^{13}C spectra of nondeuterated proteins, we verified that the ^{13}C signal disappears when the proteins are removed from the diamond (*8*).

an NV center—for instance, by activating local chemical sites using superresolution microscopy (*26*) or by placing them with a magnetized AFM tip (*27*, *28*). Though at present the inability to position the protein over a desired NV center results in long required integration times (*8*), deterministic placement, combined with a factor of ~3 improvement in coherence time, would enable detection of an individual deuteron after several seconds of integration [see (*8*), section 9].

The demonstrated technique, along with these potential improvements, may enable applications for probing the structure and dynamics of biological systems at the single-molecule level. For example, the single-molecule NMR method using quadrupolar nuclei with nuclear spin $I > 1/2$ can be used to study conformations and electrostatic environments within individual molecules. One can use the dependence of the nuclear spin level structure on the orientation of its quadrupolar axes with respect to the applied magnetic field to determine the spin's electrostatic environment (quadrupole coupling constant $\overline{Q}$ and asymmetry parameter), as well as the orientation of its molecular axes (Fig. 4A) (*19*). In our experiments (Fig. 3E), these quadrupolar shifts result in broadening of the observed spectral lines. However, if the number of nuclear spins in the molecule N_m is such that $\overline{Q}/(N_m\Delta\nu) > 1$, which ensures that the spectral range ~ $\overline{Q}$ is not overcrowded with resonances, the spectral lines associated with individual nuclei can be resolved and analyzed. As an example, Fig. 4B shows the simulated ^{2}H and ^{14}N quadrupolar spectra of a single phenylalanine molecule for two orthogonal orientations (top and upper middle panels) and two distinct conformations (two middle panels). These orientation-dependent shifts wash out in bulk NMR measurements (bottom panel). Yet unlike in bulk NMR with crystallized samples, the weights of the various single-molecule NMR resonances in a finite magnetic field (Fig. 4C) encode information about the positions of the spins within the molecule, thus allowing structural information to be deduced (*8*) regardless of the location of the target molecule.

Our approach provides a set of tools, complementary to conventional NMR, that can be

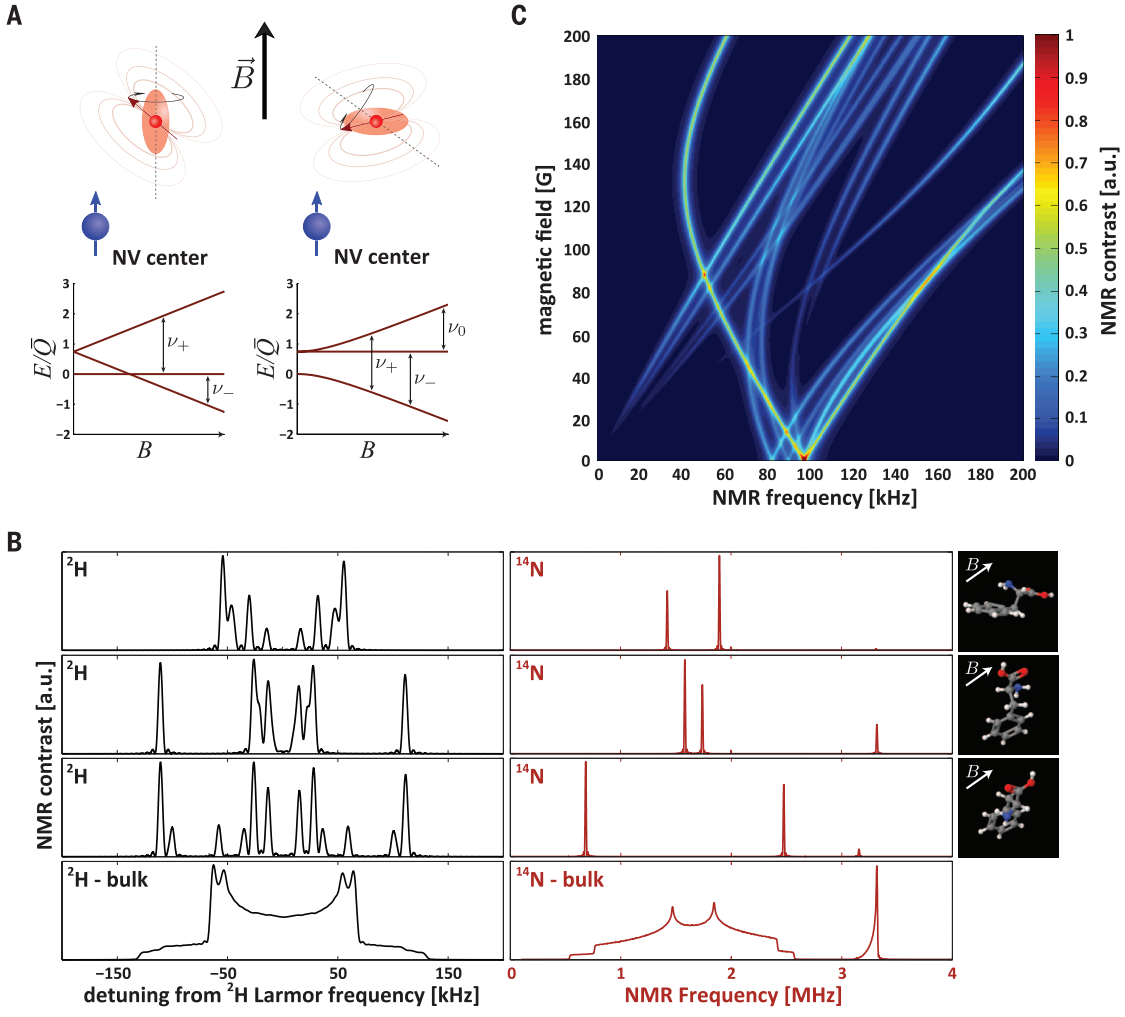


Fig. 4. Proposed analysis of individual molecules. (**A**) Orientation-dependent level structure of quadrupolar nuclear spins in an external magnetic field. The two spin-1 nuclei shown are interacting with a proximal NV center through magnetic dipole-dipole interactions. The major axes of the ellipses denote the orientation of the molecular axis. The quantization axis in each case is indicated by the dashed line. The effect of a nonzero asymmetry parameter is neglected. Allowed transitions ($\nu_\pm$ and ν_0) are indicated by arrows (*8*). *E*, energy. (**B**) Simulated quadrupolar ^{2}H and ^{14}N spectra of deuterated phenylalanine in two orthogonal orientations relative to the diamond surface (top and upper middle panels), two distinct conformations (two middle panels), and the simulated bulk spectra (bottom panels), where all possible orientations contribute equally to the spectrum. Images of phenylalanine (at right) were taken from the Protein Data Bank (PDB ID: PHE) and visualized using Jmol (www.jmol.org/). For the case of ^{2}H, only the spectral lines corresponding to $\nu_\pm$ (*8*) are shown. We assume that a magnetic field of 0.5 T is applied along the NV symmetry axis. (**C**) Magnetic field dependence of the ^{2}H spectrum corresponding to the lower middle panel at left in (B), at low magnetic field. The color bar represents NMR contrast.

used to probe the structure and dynamics of biological and chemical systems at the single-molecule level and reveal properties normally obscured in ensemble measurements. With additional improvements in sensitivity, these tools (*8*) can potentially be applicable to NMR-based label-free detection and analysis of single molecules; characterization of structural and conformational changes in systems that are not easily accessible by conventional techniques; and studies of dynamic phenomena, such as protein folding (*29*) and enzyme-substrate interactions at the single-molecule level (*30*).

REFERENCES AND NOTES

1. P. Glover, S. P. Mansfield, *Rep. Prog. Phys.* **65**, 1489–1511 (2002).
2. H. J. Mamin *et al.*, *Science* **339**, 557–560 (2013).
3. T. Staudacher *et al.*, *Science* **339**, 561–563 (2013).
4. A. O. Sushkov *et al.*, *Phys. Rev. Lett.* **113**, 197601 (2014).
5. J. M. Taylor *et al.*, *Nat. Phys.* **4**, 810–816 (2008).
6. L. Childress, R. L. Walsworth, M. D. Lukin, *Phys. Today* **67**, 38–43 (2014).
7. S. Kolkowitz, Q. P. Unterreithmeier, S. D. Bennett, M. D. Lukin, *Phys. Rev. Lett.* **109**, 137601 (2012).
8. Materials, methods, and supplementary text are available as supplementary materials on *Science* Online.
9. L. Jiang *et al.*, *Science* **326**, 267–272 (2009).
10. P. Neumann *et al.*, *Science* **329**, 542–544 (2010).
11. Y. Romach *et al.*, *Phys. Rev. Lett.* **114**, 017601 (2015).
12. Y. Chu *et al.*, *Nano Lett.* **14**, 1982–1986 (2014).
13. M. Kim *et al.*, *Appl. Phys. Lett.* **105**, 042406 (2014).
14. G. Goldstein *et al.*, *Proc. Natl. Acad. Sci. U.S.A.* **72**, 11–15 (1975).
15. S. Vijay-Kumar, C. E. Bugg, W. J. Cook, *J. Mol. Biol.* **194**, 531–544 (1987).
16. J. C. Sheehan, P. A. Cruickshank, G. L. Boshart, *J. Org. Chem.* **26**, 2525–2528 (1961).
17. A. O. Sushkov *et al.*, *Nano Lett.* **14**, 6443–6448 (2014).
18. M. Loretz, S. Pezzagna, J. Meijer, C. L. Degen, *Appl. Phys. Lett.* **104**, 033102 (2014).
19. D. B. Zax, A. Bielecki, K. W. Zilm, A. Pines, D. P. Weitekamp, *J. Chem. Phys.* **83**, 4877–4905 (1985).
20. T. P. Das, E. L. Hahn, *Nuclear Quadrupole Resonance Spectroscopy* (Academic Press, 1958).
21. B. J. Shields, Q. P. Unterreithmeier, N. P. de Leon, H. Park, M. D. Lukin, *Phys. Rev. Lett.* **114**, 136402 (2015).
22. P. London *et al.*, *Phys. Rev. Lett.* **111**, 067601 (2013).
23. T. Staudacher *et al.*, *Nat. Commun.* **6**, 8527 (2015).
24. S. Cavadini, *Prog. Nucl. Magn. Reson. Spectrosc.* **56**, 46–77 (2010).
25. A. Ajoy, U. Bissbort, M. D. Lukin, R. L. Walsworth, P. Cappellaro, *Phys. Rev. X* **5**, 011001 (2015).
26. T. A. Klar, R. Wollhofen, J. Jacak, *Phys. Scr.* **2014**, 014049 (2014).
27. D. Rugar, R. Budakian, H. J. Mamin, B. W. Chui, *Nature* **430**, 329–332 (2004).
28. C. L. Degen, M. Poggio, H. J. Mamin, C. T. Rettner, D. Rugar, *Proc. Natl. Acad. Sci. U.S.A.* **106**, 1313–1317 (2009).
29. H. S. Chung, K. McHale, J. M. Louis, W. A. Eaton, *Science* **335**, 981–984 (2012).
30. I. A. Yudushkin *et al.*, *Science* **315**, 115–119 (2007).

ACKNOWLEDGMENTS

We thank M. L. Pham, N. Chisholm, G. Kucsko, B. Harada, A. Ajoy, and P. Cappellaro for helpful discussions and experimental help. This work was supported by the Defense Advanced Research Projects Agency (QuASAR program), NSF, the Center for Ultracold Atoms, the Army Research Office Multidisciplinary University Research Initiative, the National Security Science and Engineering Faculty Fellowship program, and the Gordon and Betty Moore Foundation. I.L. was supported by the Air Force Office of Scientific Research National Defense Science and Engineering Graduate Fellowship (32 CFR 168a). Work at Ulm University was supported by the European Research Council. L.M. acknowledges support by a German Academic Exchange Service (DAAD) P.R.I.M.E. Fellowship. E.B. was supported by the Herchel Smith–Harvard Undergraduate Summer Research Program.

SUPPLEMENTARY MATERIALS

www.sciencemag.org/content/351/6275/836/suppl/DC1
Materials and Methods
Supplementary Text
Figs. S1 to S10
Table S1
References (*31*–*38*)

3 November 2015; accepted 21 January 2016
Published online 4 February 2016
10.1126/science.aad8022

NANOMATERIALS

DNA-controlled dynamic colloidal nanoparticle systems for mediating cellular interaction

Seiichi Ohta,[1,2] Dylan Glancy,[1,3] Warren C. W. Chan[1,3,4,5]*

Precise control of biosystems requires development of materials that can dynamically change physicochemical properties. Inspired by the ability of proteins to alter their conformation to mediate function, we explored the use of DNA as molecular keys to assemble and transform colloidal nanoparticle systems. The systems consist of a core nanoparticle surrounded by small satellites, the conformation of which can be transformed in response to DNA via a toe-hold displacement mechanism. The conformational changes can alter the optical properties and biological interactions of the assembled nanosystem. Photoluminescent signal is altered by changes in fluorophore-modified particle distance, whereas cellular targeting efficiency is increased 2.5 times by changing the surface display of targeting ligands. These concepts provide strategies for engineering dynamic nanotechnology systems for navigating complex biological environments.

Fundamental studies on the interactions of nanoparticle designs with biomolecules, cells, tissues, and organs are providing guiding principles with which to build nanosystems for imaging, diagnosis, and the treatment of disease. An optimal nanoparticle physicochemical property (for example, size, shape, and surface chemistry) for biological use varies with time and place within the living body, and current nanoparticle designs do not have the engineering range to meet these design requirements (*1*–*3*). For example, rod-shaped particles are reported to be preferable for tumor penetration (*4*), whereas spherical nanoparticles are better for subsequent cellular uptake by cancer cells (*5*); nanoparticles coated with polymer polyethylene glycol (PEG) can increase blood circulation time by reducing serum protein adsorption and macrophage uptake (*6*) but can impede surface-coated antibodies from cell targeting (*7*). These variations have inspired the development of interactive nanoparticle systems that can alter their properties in response to biological stimuli (*8*–*10*). However, dynamic control over the physicochemical properties of nanoparticles, especially particle shape, remains a challenge. DNA provides exquisite control and flexibility in engineering the physicochemical, morphological, optical, and electrical properties of three-dimensional (3D) nanosystems (*11*–*14*). But these DNA-assembled structures have not been fully exploited for cellular and biological application. We explored the use of DNA to assemble shape-shifting nanostructures with controlled biological function.

We used single-stranded DNA–functionalized gold nanoparticles (AuNPs) of different sizes (denoted as large, medium, and small) as building blocks to assemble shape-changing nanostructures (Fig. 1A and fig. S1). Each AuNP was functionalized with two DNA sequences: one for nanostructure assembly and the other for shape-changing (*15*). Valencies of these nanoparticles were 114, 25, and 6 DNA strands on 13-, 6-, and 3-nm AuNPs, respectively (fig. S2). The nanoparticle building blocks were assembled into "core-satellite" structures (*16*, *17*) by a linker DNA strand (L1 and L2) whose ends were complementary to two different nanoparticle types. The assembled nanostructure consists of a large core with surrounding satellites of medium and small size (Fig. 1, assembly morphology 1). An important design feature here is that the linkage between the core and the small satellites contains a single-stranded

[1]Institute of Biomaterials and Biomedical Engineering, Donnelly Center for Cellular and Biomolecular Research, University of Toronto, 164 College Street, Toronto, ON M5S 3G9, Canada. [2]Center for Disease Biology and Integrative Medicine, University of Tokyo, 7-3-1 Hongo, Bunkyo-ku, Tokyo, 113-0033, Japan. [3]Department of Chemistry, University of Toronto, 80 St. George Street, Toronto, ON M5S 3H6, Canada. [4]Department of Chemical Engineering, University of Toronto, 200 College Street, Toronto, ON M5S 3E5, Canada. [5]Department of Material Science and Engineering, University of Toronto, 160 College Street, Room 450, University of Toronto, Toronto, ON M5S 3E1, Canada.
***Corresponding author. E-mail: warren.chan@utoronto.ca**

EXTENDED PDF FORMAT
SPONSORED BY


www.rndsystems.com



Nuclear magnetic resonance detection and spectroscopy of single proteins using quantum logic

I. Lovchinsky *et al.*

Science **351**, 836 (2016);
DOI: 10.1126/science.aad8022

This copy is for your personal, non-commercial use only.

If you wish to distribute this article to others, you can order high-quality copies for your colleagues, clients, or customers by clicking here.

Permission to republish or repurpose articles or portions of articles can be obtained by following the guidelines here.

The following resources related to this article are available online at www.sciencemag.org (this information is current as of February 22, 2016):

Updated information and services, including high-resolution figures, can be found in the online version of this article at:
/content/351/6275/836.full.html

Supporting Online Material can be found at:
/content/suppl/2016/02/03/science.aad8022.DC1.html

This article **cites 35 articles**, 8 of which can be accessed free:
/content/351/6275/836.full.html#ref-list-1

This article appears in the following **subject collections:**
Physics
/cgi/collection/physics

Downloaded from on February 22, 2016

Science (print ISSN 0036-8075; online ISSN 1095-9203) is published weekly, except the last week in December, by the American Association for the Advancement of Science, 1200 New York Avenue NW, Washington, DC 20005. Copyright 2016 by the American Association for the Advancement of Science; all rights reserved. The title *Science* is a registered trademark of AAAS.